Particle acceleration in laser-driven magnetic reconnection

S. R. Totorica, T. Abel, and F. Fiuza

Articles you may be interested in

Formation of high-speed electron jets as the evidence for magnetic reconnection in laser-produced plasma
Physics of Plasmas **24**, 041406041406 (2017); 10.1063/1.4978883

Electron holes in phase space: What they are and why they matter
Physics of Plasmas **24**, 055601055601 (2017); 10.1063/1.4976854

Particle dynamics in the electron current layer in collisionless magnetic reconnection
Physics of Plasmas **23**, 102102102102 (2016); 10.1063/1.4963008

Energy conversion mechanism for electron perpendicular energy in high guide-field reconnection
Physics of Plasmas **24**, 032901032901 (2017); 10.1063/1.4977908

On the generation of magnetized collisionless shocks in the large plasma device
Physics of Plasmas **24**, 041405041405 (2017); 10.1063/1.4978882

Dynamo-driven plasmoid formation from a current-sheet instability
Physics of Plasmas **23**, 120705120705 (2016); 10.1063/1.4972218

Particle acceleration in laser-driven magnetic reconnection

S. R. Totorica,[1,2,3] T. Abel,[1,2,4] and F. Fiuza[3,a)]

[1]*Kavli Institute for Particle Astrophysics and Cosmology, Stanford University, Stanford, California 94305, USA*
[2]*Department of Physics, Stanford University, Stanford, California 94305, USA*
[3]*High Energy Density Science Division, SLAC National Accelerator Laboratory, Menlo Park, California 94025, USA*
[4]*SLAC National Accelerator Laboratory, Menlo Park, California 94025, USA*

Particle acceleration induced by magnetic reconnection is thought to be a promising candidate for producing the nonthermal emissions associated with explosive phenomena such as solar flares, pulsar wind nebulae, and jets from active galactic nuclei. Laboratory experiments can play an important role in the study of the detailed microphysics of magnetic reconnection and the dominant particle acceleration mechanisms. We have used two- and three-dimensional particle-in-cell simulations to study particle acceleration in high Lundquist number reconnection regimes associated with laser-driven plasma experiments. For current experimental conditions, we show that nonthermal electrons can be accelerated to energies more than an order of magnitude larger than the initial thermal energy. The nonthermal electrons gain their energy mainly from the reconnection electric field near the X points, and particle injection into the reconnection layer and escape from the finite system establish a distribution of energies that resembles a power-law spectrum. Energetic electrons can also become trapped inside the plasmoids that form in the current layer and gain additional energy from the electric field arising from the motion of the plasmoid. We compare simulations for finite and infinite periodic systems to demonstrate the importance of particle escape on the shape of the spectrum. Based on our findings, we provide an analytical estimate of the maximum electron energy and threshold condition for observing suprathermal electron acceleration in terms of experimentally tunable parameters. We also discuss experimental signatures, including the angular distribution of the accelerated particles, and construct synthetic detector spectra. These results open the way for novel experimental studies of particle acceleration induced by reconnection. *Published by AIP Publishing.* [http://dx.doi.org/10.1063/1.4978627]

I. INTRODUCTION

Magnetic reconnection is a fundamental plasma process that converts magnetic field energy into plasma energy through the breaking and rearrangement of magnetic field lines.[1] The energy released as the magnetic field changes topology drives plasma flows, heats the plasma, and accelerates energetic particles. Reconnection is important in the dynamics of magnetized plasmas in space physics, astrophysics, and laboratory nuclear fusion devices.[2–4] It is believed to play a key role in frontier problems in physics, including the origin of cosmic rays, and is also relevant for applications such as space weather and nuclear fusion energy. Observations of explosive events in astrophysics and space physics, such as solar flares, pulsar wind nebulae, gamma-ray bursts, and jets from active galactic nuclei, often indicate rapid energy dissipation and efficient particle acceleration, and these systems are likely composed of magnetized plasma. Reconnection is a promising candidate to explain the fast and efficient dissipation of magnetic energy and the production of the nonthermal particle distributions inferred to be present in these systems.[5]

Recently, several groups have used numerical simulations to investigate the particle acceleration properties of reconnection over the large range of conditions spanned by systems where reconnection is expected to play an important role.[6–12] The environment in many magnetized astrophysical outflows of interest is expected to be in the relativistic regime, where the magnetization parameter $\sigma = B^2/4\pi n_i m_i c^2$ is greater than one, meaning that the magnetic energy per particle exceeds the rest mass energy. Studies in this regime have clearly shown that relativistic reconnection is an efficient mechanism for converting magnetic energy into relativistic nonthermal particles. These energetic particles contain the majority of the total energy released, and the energy spectra show power-laws with hard slopes that can approach 1 for large σ.[6,7] In the non-relativistic regime, reconnection has been shown to energize nonthermal populations of particles, but it is not clear whether the resulting energy spectra form power-laws.[8–12]

These studies have identified many distinct acceleration mechanisms. The points where the reconnecting magnetic field vanishes are known as X points, and here the particles are unmagnetized and can be freely accelerated by the electric field associated with reconnection. Magnetic island structures known as plasmoids form as a result of the current sheet tearing instability,[13] and these can have important consequences for the particle acceleration. Particles can be accelerated by a first-order Fermi process as they bounce

a)Electronic mail: fiuza@slac.stanford.edu

between the ends of a contracting plasmoid,[11] and they can also be accelerated in secondary reconnection layers that form as two plasmoids merge together.[8] The relative importance of these processes and which are responsible for forming the power-law is not fully understood. It is also important to note that the majority of the studies of particle acceleration and reconnection use the kinetic Harris equilibrium as initial conditions and employ fully periodic boundary conditions. These very idealized initial conditions include a preformed current sheet, and recent simulations without preformed current sheets have shown important differences such as significantly softer spectral indices.[14] It thus remains an active area of research to determine the efficiency of reconnection in accelerating nonthermal particles and how this depends on the plasma conditions. The ability to study this process in a finite sized laboratory system with relevant plasma conditions would be very valuable for advancing our understanding of reconnection and determining whether it can account for observational data.

High energy laser facilities, such as the OMEGA laser at the University of Rochester and the National Ignition Facility at Lawrence Livermore National Laboratory, can focus kJ to MJ energies onto sub-millimeter spot sizes over nanosecond time scales and create high-energy-density (HED) plasma states in the laboratory. These lasers can ablate plasmas with keV temperatures when focused onto solid targets. While the spatial and temporal scales of laboratory plasmas are extremely different from those in astrophysical systems, the plasma conditions produced can reach a regime where Ohmic dissipation is negligible and the governing equations are invariant under scaling transformations.[15,16] This allows the design

of laboratory experiments whose results can be used for the interpretation of astrophysical phenomena, which has given rise to the field of HED laboratory astrophysics.[17] Over the past ten years several experiments have been performed using laser-driven HED plasmas to study magnetic reconnection in the laboratory.[18–26] For a review of laboratory reconnection experiments see Ref. 27. By focusing kilojoule per nanosecond lasers onto solid targets, expanding plasma bubbles are produced that self-generate megagauss scale toroidal magnetic fields due to misaligned density and temperature gradients (the Biermann battery $\nabla n \times \nabla T$ mechanism[28–30]). The expansion of two nearby plasma bubbles can then drive reconnection between these self generated magnetic fields, or alternatively an externally imposed magnetic field can be used[24] (Fig. 1(a)). Diagnostics such as proton radiography and Thompson scattering allow the detailed measurement of the magnetic field and plasma conditions during the experiments. Several prominent features of reconnection have been observed in these experiments, including changes in magnetic field topology,[19] plasma heating,[23] and the formation of plasma jets.[18] Reconnection in laser-driven plasmas takes place in a strongly driven regime, where the inflow speeds are larger than both the Alfvén and sound speeds. The high Lundquist number and large system size relative to the ion inertial length allows a comparison with astrophysical systems via the previously mentioned scaling laws. However, it has remained unclear whether nonthermal particle acceleration could be studied in these systems, and this is one of the most important signatures of reconnection for connecting to systems in astrophysics.

In this manuscript, we investigate the particle acceleration properties of magnetic reconnection in laser-driven
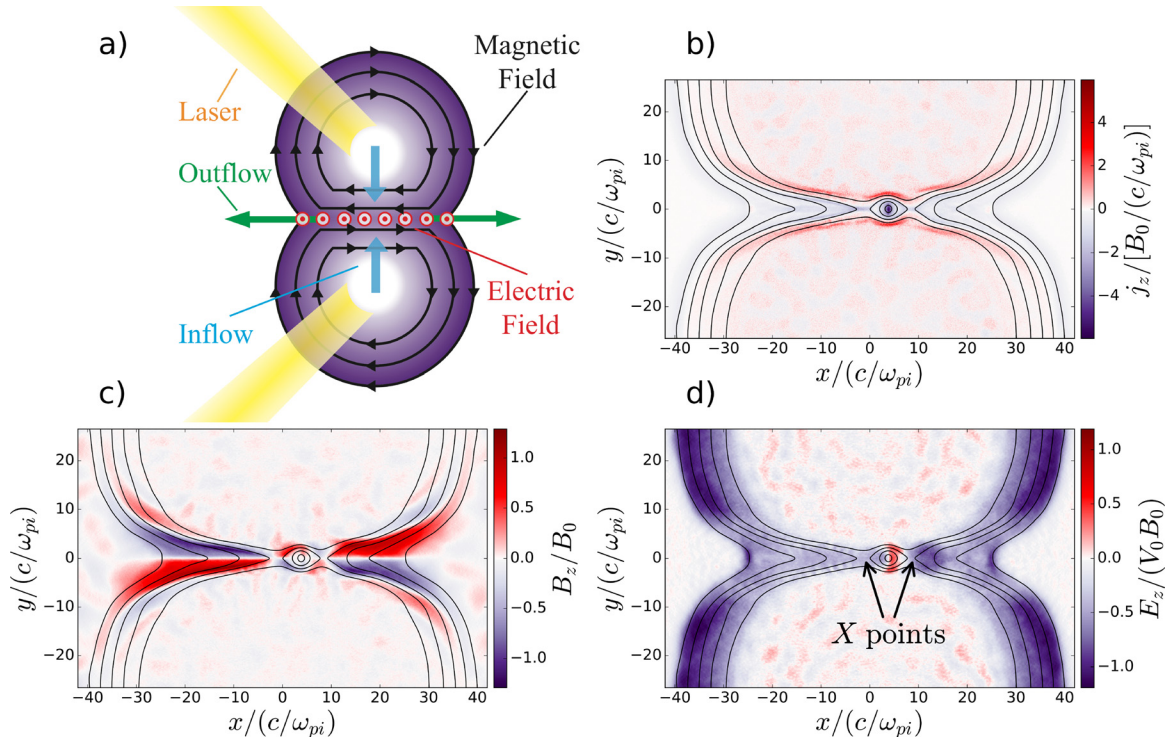

FIG. 1. (a) Experimental geometry of magnetic reconnection in laser-driven plasmas. (b) Out-of-plane current j_z, with overlaid magnetic field lines. (c) Out-of-plane magnetic field B_z, showing the quadrupolar signature of Hall-mediated reconnection. (d) Out-of-plane electric field E_z, showing the motional electric field in the body of the bubble and the reconnection electric field at the X points.

plasmas by means of *ab initio* particle-in-cell (PIC) simulations. Using the fully relativistic, state-of-the-art PIC code OSIRIS[31–34] we perform two-dimensional (2D) and three-dimensional (3D) simulations in the conditions and geometries of laser-driven reconnection experiments. We find that in the conditions of current experiments, nonthermal electrons can be accelerated to energies more than an order of magnitude larger than the initial thermal energy. The electrons are energized primarily by direct acceleration from the reconnection electric field at the X points, and the randomness associated with particle injection and escape from the finite-sized system gives rise to a nonthermal component with a power-law shape. Simulations for the same plasma conditions but with an infinite periodic system transverse to the direction of the flows show a shallower nonthermal component that extends to higher energies, demonstrating the impact of particle escape on the shape of the spectrum. Electrons can also become trapped in plasmoids and gain further energy at a slower rate due to the drifting motion of the plasmoid. Based on these results we derive an analytical estimate for the maximum electron energy and a threshold condition for suprathermal energization in terms of experimentally tunable parameters. We investigate the experimental signatures by considering the angular distribution of the energetic electron velocities and construct synthetic spectra for detectors placed at various orientations with respect to the system, which show that energetic electrons are emitted in the direction of the reconnection outflows and antiparallel to the reconnection electric field. This manuscript presents a more detailed analysis of recently published results on particle acceleration in laser-driven reconnection,[35] and expands on this original study by presenting new results on the influence of particle escape and a consideration of experimental signatures.

The outline of this manuscript is as follows. The details of the numerical system and the initial conditions of the simulations are given in Section II. In Section III, we analyze the 2D simulations in detail and investigate the electron energy spectrum and acceleration mechanisms, discussing the roles of the X points as well as Fermi and betatron acceleration. We then consider 3D effects, particle escape from the finite system, and the impact of numerical parameters. We consider the experimental detection in Section IV and in Section V we summarize our conclusions.

II. DESCRIPTION OF SIMULATIONS

To model laser-driven reconnection experiments we use the particle-in-cell (PIC) method, where the plasma is represented by a finite number of discrete simulation particles in position and velocity space.[36] A discrete current density is calculated by weighting the particle positions and velocities onto a grid that covers the spatial domain. This current density is then used in Maxwell's equations to solve for the electric and magnetic fields, also defined on discrete grids that cover the spatial domain. The electric and magnetic fields are then weighted to each particle's position to calculate the Lorentz force used to update that particle's velocity and position, and the simulation proceeds in this way in a series of

time steps. In the PIC method short-range Coulomb forces are greatly reduced by the use of finite-size particles, which is ideal for the modeling of collisionless plasmas. Coulomb collisions can be taken into account in PIC simulations through the use of a binary Monte Carlo collision operator.[37,38] For this initial study we restrict the simulations to the collisionless case; the influence of collisionality on the particle acceleration will be the subject of future work. This is partially justified by the fact that many of the HED laser-plasma experiments of interest to our study, where keV temperatures and 1000 km/s flow velocities are reached, have particle mean free paths that are comparable or larger than the system size. PIC simulations have played an important role in guiding and interpreting the results of previous experiments, and the goal of our study was to use this method to investigate whether these experiments could be used to study nonthermal particle energization resulting from reconnection.

The initial conditions of the simulations correspond to a time partway through the experiment, when the two magnetized plasma bubbles are expanding and about to interact. These initial conditions do not model the initial generation of the plasma or magnetic field but do capture many features of the system likely to influence the particle acceleration, including the finite size which allows particles to escape the system and the driven inflows. These generic initial conditions can be connected to a number of experimental geometries,[39] including both self-generated and externally imposed magnetic fields, and are consistent with previous PIC studies of laser-driven reconnection.[40–43]

The centers of the plasma bubbles are given by the vectors $\mathbf{R}^{(1)} = (0, R, 0)$ and $\mathbf{R}^{(2)} = (0, -R, 0)$. The corresponding radial vectors from the bubble centers are $\mathbf{r}^{(i)} = \mathbf{r} - \mathbf{R}^{(i)}$, where R is the radius of each bubble when they begin to interact. The initial density profile is given by $n_b + n^{(1)} + n^{(2)}$ where $n^{(i)}(r^{(i)}) = (n_0 - n_b) \cos^2(\frac{\pi r^{(i)}}{2R_0})$ if $r^{(i)} < R_0$, 0 otherwise. Here, $n_b = 0.01 n_0$ is the density of the background plasma, and R_0 is the bubble radius at the beginning of the simulation, which we typically take to be $0.9 - 1.0R$. An initial velocity profile is given to each bubble to initiate the expansion, which is given by $\mathbf{V}^{(1)} + \mathbf{V}^{(2)}$ where $\mathbf{V}^{(i)}(r^{(i)}) = V_0 \sin(\frac{\pi r^{(i)}}{R_0})\mathbf{r}^{(i)}$ if $r^{(i)} < R_0$, 0 otherwise. The initial magnetic field corresponds to the sum of two oppositely aligned ribbons, $\mathbf{B}^{(1)} + \mathbf{B}^{(2)}$, where $\mathbf{B}^{(i)}(r^{(i)}) = B_0 f(\theta^{(i)}) \sin(\frac{\pi(R_0 - r^{(i)})}{2L_B})\hat{\phi}^{(i)}$ if $R_0 - 2L_B \leq r^{(i)} \leq R_0$, 0 otherwise. Here $L_B = R_0/4$ is the initial half-width of the magnetic field ribbon, and $\theta^{(i)}$ and $\phi^{(i)}$ are the polar and azimuthal angles, respectively, of spherical coordinate systems originating at the bubble centers. The 2D simulations model the plane parallel to the magnetic field and containing the centers of the bubbles; in this case, $\theta^{(i)} = \pi/2$ and $f(\theta^{(i)}) = 1$. For the 3D simulations, $f(\theta^{(i)})$ is zero near the z-axis, rises from 0 to 1 from $\theta^{(i)} = \pi/16$ to $\theta^{(i)} = 2\pi/16$, and similarly from $\theta^{(i)} = 15\pi/16$ to $\theta^{(i)} = 14\pi/16$. The rise is given by the polynomial $10x^3 - 15x^4 + 6x^5$ which approximates a Gaussian shape. This configuration is divergence free and consists of magnetic field loops that are parallel to the x-y

plane. For the case of reconnection between self-generated magnetic fields, these initial conditions are idealized and neglect small-scale field structures that can arise. In particular, recent work has suggested the possibility of coupling with electron scale kinetic instabilities.[44,45] We note that for typical laser-ablated plasma conditions (e.g., at OMEGA or OMEGA EP[19,24–26,40,41]), where near the foils we have $T_e \sim 100$ eV and $n_e \sim 10^{21} - 10^{22}$ cm^{-3}, the electron collisional mean free path is $\sim 0.03 - 0.3 \mu m$, which is of the order of or smaller than the electron skin depth. It is thus not clear whether electron scale instabilities can develop for such conditions. However, this deserves more detailed investigation that is beyond the scope of the current work. The electric field is initialized as $\mathbf{E} = -\mathbf{V} \times \mathbf{B}/c$, consistent with the initial motion of the magnetized plasma, where $\mathbf{V} = \mathbf{V}_e = \mathbf{V}_i$ at $t = 0$. An initial out-of-plane current J_z is included that is consistent with $\nabla \times \mathbf{B} = \frac{4\pi}{c}\mathbf{J}$ and distributed to the electrons and ions by the inverse of their mass ratio. The majority of the simulations use a box of size $8R \times 2R$ evolved to $t/t_d = 0.5$ for 2D, and a box of size $4R \times 2R \times 4R$ evolved to $t/t_d = 0.25$ for 3D. Here $t_d = R/V_0$ is the relevant timescale for the interaction and the experimental measurements. The boundaries along the outflow directions, x (and z for 3D), are thermal re-emitting for the background plasma particles, absorbing for the plasma bubble particles, and an absorbing layer[46] for the electromagnetic fields. The anti-symmetry of the system allows the use of periodic boundaries along the inflow (y) direction. We also perform simulations with larger domains and without periodic boundaries along the inflow direction (i.e., modeling the entire bubbles) which confirm that the boundaries are not significantly affecting the results. The open boundaries for the plasma bubble particles and the electromagnetic fields prevent energetic particles and radiation from the reconnection outflows from artificially recirculating in the system. Many of the previous reconnection simulation studies use periodic boundaries in the direction of the reconnection outflows and thus may suffer unphysical effects from recirculating particles and radiation. If particle acceleration could be studied in the finite-sized systems of laser-driven plasmas it would yield critical insight for understanding the role of boundary conditions and particle escape in models of reconnection.

To enable a study of the particle acceleration process without the effects of particle escape from the finite sized system, in Sec. III G we also use an idealized 2D configuration where the plasma flows are infinite and periodic transverse to the flow. This corresponds to the same initial conditions as described above, but with the radial vectors changed to $\mathbf{r}^{(1)} = (0, y - R, 0)$ and $\mathbf{r}^{(2)} = (0, y + R, 0)$. These simulations use a spatial domain of size $2L_x \times 2L_y \approx 53c/\omega_{pi} \times 53c/\omega_{pi}$ and fully periodic boundary conditions. We further simplify this system in Sec. III E by assuming uniformity along the x-direction, which suppresses reconnection and allows us to isolate the process of betatron acceleration.

To model the plasma conditions relevant for recent laser-driven reconnection experiments (e.g., those generated with the OMEGA EP laser[24]) we directly match many of the plasma parameters to their laboratory values. See Table I for

TABLE I. Values of the dimensionless plasma parameters estimated from recent experimental measurements[41] and for the simulations studied in this manuscript. Here $S = LV_A/\eta$ is the Lundquist number. * While PIC simulations nominally model collisionless systems, in reality a finite numerical collisionality arises from the discrete nature of the simulation particles.

Parameter	Experimental	Simulation
M_S	0.65–2	2–8
M_A	1.3–20	4–64
B	8–150	8–128
$R/(c/\omega_{pi})$	10–80	20–26.5
S	80–200	∞^*

values of the dimensionless plasma parameters estimated from recent experimental measurements[41] and for the simulations studied below. We model a range of Alfvénic and sonic Mach numbers within the experimentally accessible range, $M_A = V_0/V_A = 4 - 64$ and $M_S = V_0/C_S = 2 - 8$, where $V_A = B_0/\sqrt{4\pi n_0 m_i}$ is the Alfvén speed and $C_S = \sqrt{ZT_e/m_i}$ is the sound speed. We also match the high experimental plasma beta, which characterizes the dynamical importance of the magnetic field, $\beta_e = \frac{n_0 T_e}{B_0^2/8\pi} = 2\left(\frac{M_A}{M_S}\right)^2 = 8 - 128$. The bubble radii at the time of interaction are chosen to be $R/(c/\omega_{pi}) \simeq 26.5$ for the 2D simulations and $R/(c/\omega_{pi}) \simeq 20 - 26.5$ for the 3D simulations, which are within the experimentally accessible range[41] of $R/(c/\omega_{pi}) = 10 - 100$. The initial temperatures T_e and T_i are taken to be equal and uniform throughout the plasma. Due to computational expense, the parameters C_S/c and $m_i/m_e Z$ (where c is the speed of light, m_i and m_e the ion and electron masses, and Z the ion charge) are not directly matched to experimental values. Instead, in the majority of the simulations we use $V_0/c = 0.1$ and $m_i/m_e Z = 128$, with C_S chosen to correctly match M_S. Using artificial values for these parameters is a commonly used approximation that effectively reduces the speed of light and increases the electron mass, but can still allow for an adequate separation of the relevant temporal and spatial scales to accurately model the physical processes. In Sec. III G we show how we have varied these parameters in the range of $V_0/c = 0.025 - 0.1$ and $m_i/m_e Z = 32 - 512$ to verify that the main results of this study are relatively insensitive to their exact values. The field quantities are represented on a spatial grid with a resolution of $\Delta x = 0.5c/\omega_{pe} \simeq 0.04c/\omega_{pi}$ and cubic interpolation is used to weight between the particle and field quantities. The 2D simulations use a timestep of $\Delta t = 0.35 \omega_{pe}^{-1}$ and 64 particles per cell per species, whereas the 3D simulations use a timestep of $\Delta t = 0.285 \omega_{pe}^{-1}$ and 8 particles per cell per species.

III. SIMULATION RESULTS

A. General features

To illustrate the main results, we use as a representative case of the 2D simulation with $M_S = 2$ and $M_A = 4$ and analyze it in detail. The overall evolution of the system is consistent with previous PIC studies using similar initial conditions.[40–43] As the plasma flows carry the magnetic flux into the interaction region at super-Alfvénic speeds, the

plasma is compressed by the ram pressure and the amplitude of the magnetic field increases by a factor of ≈ 1.65. A current sheet forms (Fig. 1(b)) with a width on the order of the ion skin depth, c/ω_{pi}, which is the scale at which electrons and ions decouple. This decoupling enables fast reconnection mediated by the Hall effect,[47] and the quadrupolar out-of-plane magnetic field signature of Hall reconnection is clearly visible in the fields (Fig. 1(c)). The current sheet is then unstable to the tearing instability and a single plasmoid is formed that slowly drifts in the direction of the reconnection outflows as reconnection proceeds. The formation of a single plasmoid is consistent with linear theory for the tearing instability[48] which predicts the fastest growing mode to be given by $k_{max}\delta = 0.55$, where $\delta \approx 1.41\, c/\omega_{pi}$ is the half-width of the current sheet measured in the simulation. For the range of Alfvénic and sonic mach numbers simulated we typically observe magnetic field enhancement by a factor of 1.5–5 and the formation of 1–3 plasmoids.

An out-of-plane electric field is present in the current sheet (Fig. 1(d)), and we have calculated the various terms in the generalized Ohms law ($\mathbf{E} = -\frac{1}{c}\frac{n_i}{n_e}\mathbf{v}_i \times \mathbf{B} + \frac{1}{en_ec}\mathbf{J} \times \mathbf{B} - \frac{\nabla \cdot \mathbf{P}_e}{en_e} - \frac{m_e}{e}\frac{d\mathbf{v}_e}{dt}$) to confirm that the electric field in the diffusion region is predominantly supported by the Hall and off-diagonal electron pressure tensor terms. This is in agreement with previous kinetic studies of reconnection starting from the Harris equilibrium[47] and laser-driven reconnection.[40] At the X points, where the magnetic field vanishes, this electric field is almost completely supported by the off-diagonal electron pressure tensor terms and can be identified as the reconnection electric field; this is distinct from the motional electric field that arises from the expansion of the magnetized plasma bubble, which is self-consistently included in

our initial conditions. We observe the typical value of the reconnection electric field in the diffusion region to be $E \approx 0.5V_0B_0$. In terms of the local Alfvén speed and compressed magnetic field, we find $E \approx 0.3V_AB$ at $t/t_d = 0.25$, when the plasmoid is just beginning to form, which is similar to the reconnection rates typically measured in simulations of collisionless reconnection.[47]

After the onset of reconnection, the reconnected field lines drive plasma outflows that escape the interaction region due to the finite size of the system, similar to the jets that have been measured in the experiments. An in-plane polarization electric field directed away from the plasma bubbles is set up as the hot electrons expand faster than the ions (Figs. 2(a) and 2(b)). For the system size and magnetic field strength of this simulation, the electrons are strongly magnetized, whereas the ions are not. This is visible in Figs. 2(c) and 2(d) which show the longitudinal component of the momentum, p_y, as a function of the y-axis for the ions and the electrons. The ions are able to easily penetrate across the interaction region whereas the electrons are strongly affected by the magnetic field.

B. Electron spectrum

Figure 3(a) shows the temporal evolution of the electron energy spectrum, with the different colored lines corresponding to the spectrum at equally spaced times throughout the duration of the simulation, showing the clear development of a high energy component that resembles a steep power-law with energies extending up to $\approx 50\, k_BT_e$. In Figure 3(b) we fit the low-energy portion of the electron spectrum at $t/t_d = 0.25$ to a Maxwell–Boltzmann distribution, and observe that the
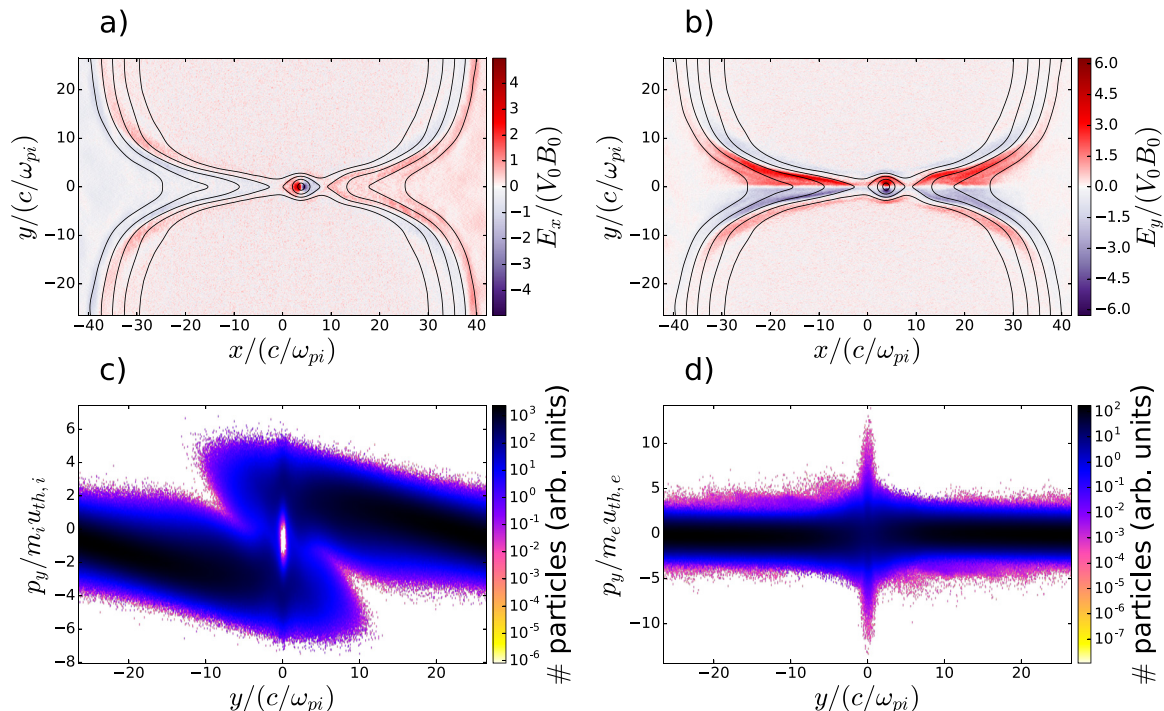

FIG. 2. (a) E_x and (b) E_y, showing the in-plane polarization electric field resulting from the expansion of the hot electrons. Longitudinal momentum p_y along the direction of the reconnection inflows for (c) ions, showing the interpenetration of the streams and (d) electrons, showing that the electrons are strongly affected by the magnetic field in the interaction region.
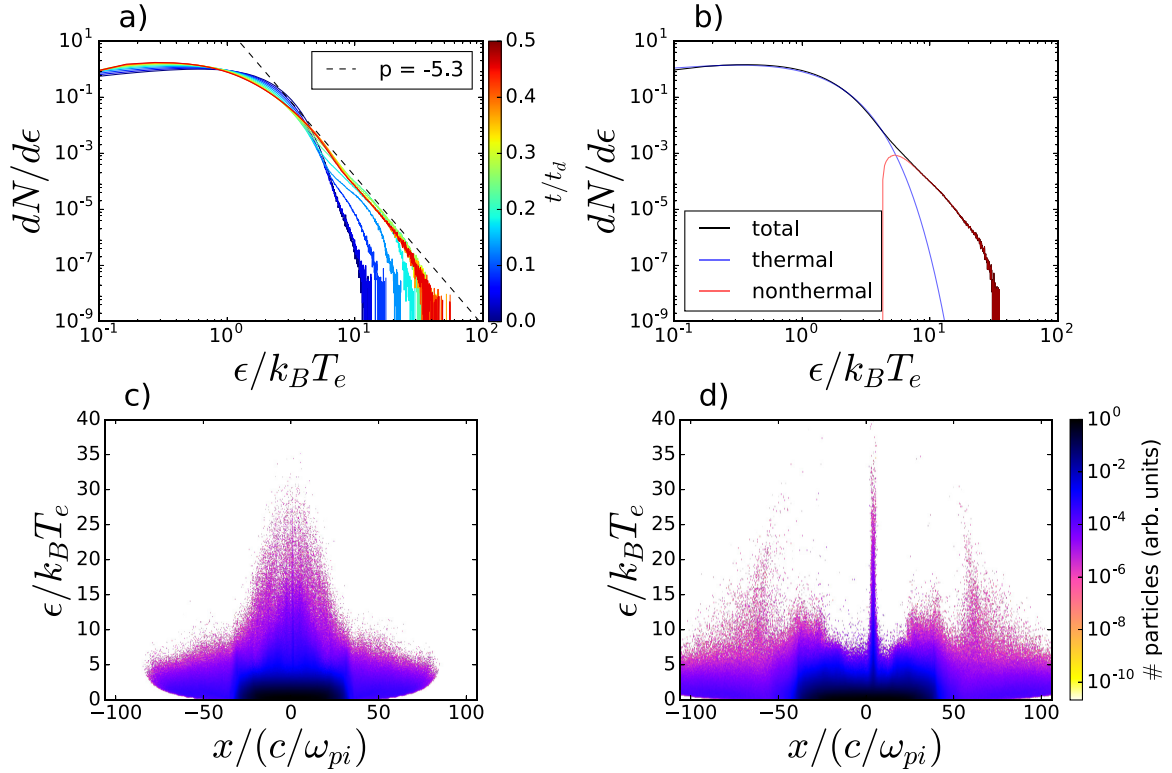
FIG. 3. (a) Temporal evolution of the electron energy spectrum, with a power-law of index $p = -5.3$ plotted for reference (dashed line). (b) Best fit of the low energy portion of the spectrum to a Maxwell–Boltzmann distribution, and the remaining nonthermal component. Distribution of electron energies along the direction of the reconnection outflows at (c) $t/t_d = 0.25$ and (d) $t/t_d = 0.5$.

remaining nonthermal component resembles a power-law with an index of ~5.3 that starts at $\sim5k_BT_e$ and with an exponential cutoff at $\sim20k_BT_e$. At the end of the simulation ($t/t_d = 0.5$), the nonthermal component contains $\sim8\%$ of the initial energy of the electrons that reach the interaction region, $\sim24\%$ of the energy stored in the initial magnetic field, and $\sim1\%$ of the total number of electrons initially in the bubbles.

Figures 3(c) and 3(d) show the distribution of electron energies along the direction of the reconnection outflows at $t/t_d = 0.25$ and 0.5, respectively. In Figure 3(c) there is a broad peak centered near x = 0, which is approximately the location of the X point before the plasmoid forms. Figure 3(d) shows a later time, after the plasmoid has formed, where energetic electrons are seen both to escape in the direction of the reconnection outflows and to become localized near the position of the single plasmoid that forms. At this time the most energetic electrons in the system are seen to be inside the plasmoid. In a realistic 3D system (which we discuss below) the electrons trapped inside the plasmoid would also eventually escape the reconnection region, but orthogonal to the reconnection plane along the z-direction.

C. Acceleration mechanism

To determine the acceleration mechanism responsible for producing the high energy tail, we have tracked the detailed motion of the electrons that attain the highest energy by the end of the simulation. This has revealed two main distinct types of behavior, which are illustrated in Figs. 4(a) and 4(b) by representative example electron trajectories plotted over the magnitude of the in-plane magnetic field.

Figure 4(a) shows the magnetic field at an early time ($t/t_d = 0.25$), Fig. 4(b) shows a later time after the plasmoid has formed ($t/t_d = 0.5$), and the diamonds show the initial position of the electrons. The inlays show the energy of the electrons as a function of position along the x-axis, which shows that in both cases the electrons gain the majority of their energy in a narrow region along the x-axis. This corresponds to when they interact with an X point, where the magnetic field vanishes and the unmagnetized electrons can be freely accelerated. To separate the contributions to the energization from the out-of-plane reconnection electric field and the in-plane polarization electric field, we have calculated the work done on the electron by each electric field component individually throughout the simulation as $W_i = \int_0^t dt'(p_i/\gamma m_e)(-e E_i)$. The evolution of the total energy and the work done by each electric field component for the two example electrons is plotted in Figs. 4(c) and 4(d). These plots show that it is the out-of-plane component of the electric field associated with reconnection at the X points that is primarily responsible for energizing the electrons. As the electrons oscillate inside the current sheet, they alternately gain and lose energy from the polarization electric field, which leads to the oscillations seen in the total energy superimposed over the growth from the reconnection electric field. After the electrons have acquired a large out-of-plane velocity, the in-plane magnetic field rotates their velocities into the plane where the electrons will either escape the system (Figure 4(a)), become trapped inside a plasmoid (Figure 4(b)), or continue to travel along the field lines circling the bubbles. The example electron that leaves
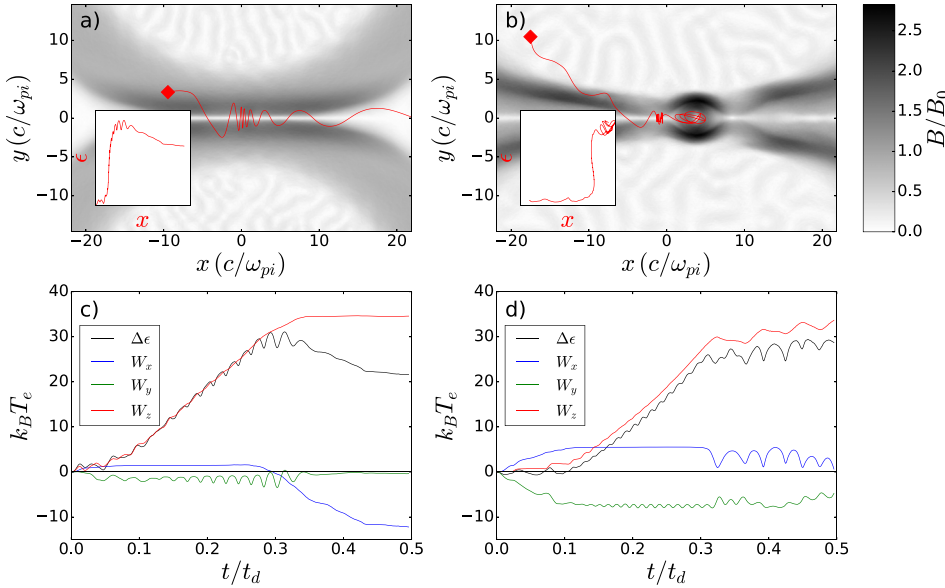
FIG. 4. (a) Trajectory of an escaping electron, plotted over the magnitude of the magnetic field at $t/t_d = 0.25$, and (b) trajectory of a trapped electron, plotted over the magnitude of the magnetic field at $t/t_d = 0.5$. Inlays show each electron's energy as a function of its position along the x-axis. (c) and (d) The temporal evolution of the total change in energy and the work done by each electric field component for the electrons in (a) and (b), respectively.

the system loses some of its energy when it escapes as it crosses the polarization electric field (Figure 4(c)), whereas the electron that becomes trapped inside the plasmoid gains further energy but at a slower rate (Figure 4(d)).

The energization inside the plasmoid is due to the drift motion of the plasmoid in the direction of the reconnection outflows, which leads to the trapped electrons being exposed to an out-of-plane motional electric field with alternating polarity (Figure 1(c)) as they circle inside the plasmoid.[8] Plasma flowing into the drifting plasmoid from the bounding X points reduces the bulk flow velocity on one side and increases it on the other. The net result is that the trapped electrons are exposed to an average field in the same direction as the reconnection electric field over each approximately circular orbit inside the plasmoid, allowing them to gain further energy. Other particle tracks also show that the energy gain from the direct acceleration at the X points is much more significant than the energy gain inside the plasmoid, and this slow energization is not seen to change the shape of the spectrum significantly. We also note that we have simulated the expansion of a single plasma bubble to confirm that the motional electric field arising from the bubble expansion alone does not significantly energize particles.

D. Fermi acceleration

Previous work has shown that the presence of plasmoids in the current sheet may give rise to Fermi-acceleration processes that can lead to power-law energy spectra.[11] However, for the conditions of our simulations, direct acceleration by the reconnection electric field at the X points is the primary energization mechanism, rather than the interaction with plasmoids which only leads to a small energy gain. The acceleration while trapped inside a single plasmoid can be considered as a series of Fermi type B reflections,[49] but is not a stochastic acceleration process (e.g., diffusive shock acceleration). Significant Fermi acceleration from the interaction with multiple plasmoids is likely to require a larger system size with a larger number of plasmoids and thus a

more energetic laser drive than that used in current experiments. Our simulation results thus indicate that the power-law is the result of direct acceleration at X points rather than interaction with plasmoids. A power-law may result as the electrons are injected into the current layer at varied distances from the X points. They will then be accelerated by the reconnection electric field for varied amounts of time before the in-plane magnetic fields direct them out of the diffusion region, establishing a distribution of energies.[7] This argument is supported by calculating the spectrum of the electrons in the plasmoid and subtracting it from the spectrum including all electrons, as shown in Fig. 5. The high energy tail has a similar shape for the electrons inside and outside of the plasmoid, indicating that it is established by the initial acceleration at the X points rather than through interaction with the plasmoid.

E. Betatron acceleration

In addition to the energization resulting from reconnection, the electrons can also be energized by betatron acceleration[50] as a result of the compression of the magnetic field as the plasma bubbles expand into each other. This contribution to the acceleration can be isolated by performing 1D simulations with the configuration described in Sec. II, where the particles are constrained to move only along the y-axis and the system is assumed to be uniform along the x- and z-directions. In this case, the magnetic field is still compressed as the flows expand, but the uniformity along the x-direction suppresses reconnection. Figure 6(a) shows the evolution of the energy of an electron as a function of its position along the y-axis, which is representative of the energized electrons in the simulations and illustrates the energy gain from the betatron acceleration process. The electron gains energy primarily during reflections rather than at the center of the current sheet. As the magnetic field enhancement saturates, the betatron acceleration becomes negligible. Figure 6(b) shows a similar plot for an electron from a 2D simulation where reconnection does occur. This plot reveals three phases to
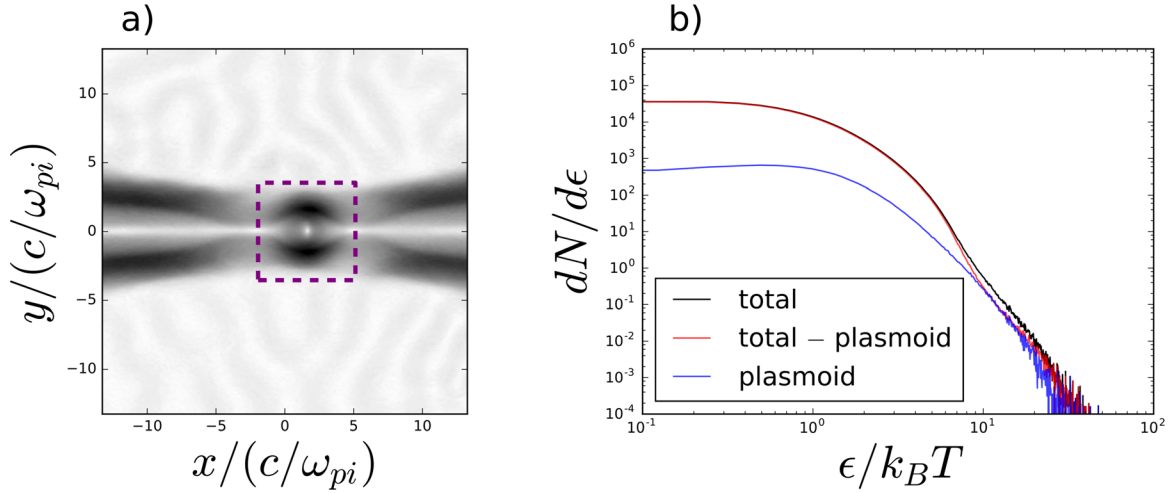
FIG. 5. (a) Magnetic field amplitude, with a box showing the region used for calculating the plasmoid spectrum. (b) Electron energy spectrum including all electrons (total), only electrons outside the box in (a) (total-plasmoid), and only those inside the box in (a) (plasmoid).

the acceleration. Initially, the particle gains a small amount of energy by betatron acceleration (region I). Once reconnection initiates, the particle interacts with an X point and gains energy from the reconnection electric field, which is clearly visible as a nonzero slope when the particle is at the center of the current sheet (region II). The final phase shows the small net energy gain once the particle has entered the plasmoid (region III). For the conditions of our simulations, X point acceleration is the dominant energization mechanism, as can be seen in Figure 6(b). For different plasma conditions, betatron acceleration may be the dominant acceleration mechanism.[51] A detailed study of the relative importance of X point, betatron, and plasmoid related acceleration mechanisms and how this depends on the plasma conditions will be the subject of future work.

F. 3D effects

This 2D model system does not capture the finite size of the system in the out-of-plane direction. As this is also the

direction the electrons are accelerated along, it is critical to consider the 3D effects. Using the initialization described in Sec. II, we have performed full 3D simulations of reconnection between expanding plasma bubbles for the conditions $M_S = 2$, $M_A = 4$, and $R/(c/\omega_{pi}) \simeq 20$. Figure 7(a) shows the electron energy spectrum at $t/t_d = 0.25$, which exhibits a high-energy tail with a similar shape to the 2D case, suggesting that the acceleration mechanisms are similar in 2D and 3D. An important difference is that the maximum electron energy is smaller for the 3D case, which is due to the finite out-of-plane size limiting the distance over which the electrons can be accelerated by the reconnection electric field to approximately the diameter of the bubble.

To derive a scaling of the maximum electron energy as a function of the plasma conditions, we first determine the effective electric field accelerating the electrons by analyzing four 2D simulations and one 3D simulation with $M_S = 2$ and M_A ranging from 4 to 32. Figure 7 shows a comparison of the electron energy spectra at $t/t_d = 0.25$ for some of these simulations. The increase in maximum electron energy with
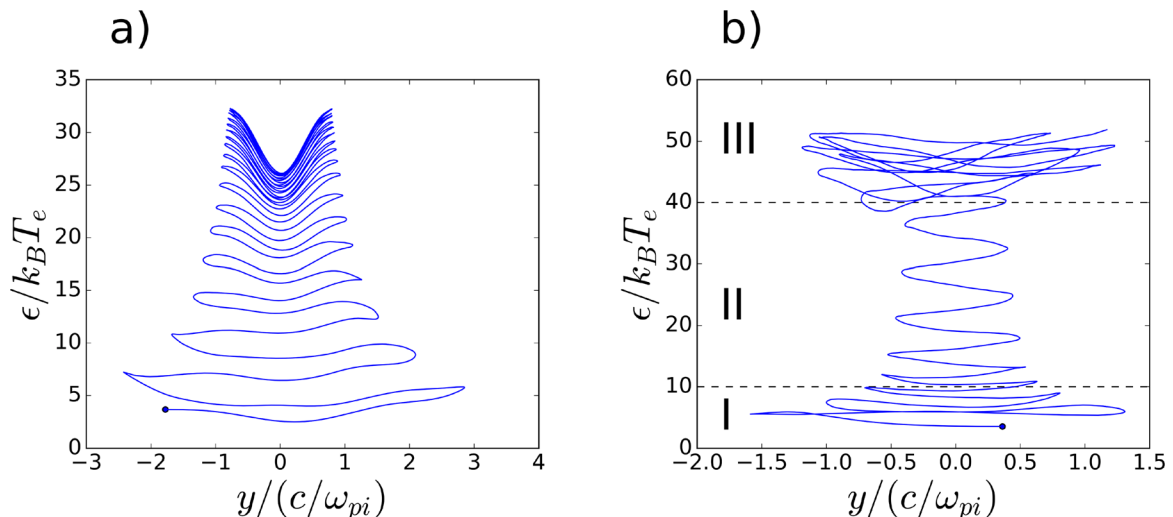

FIG. 6. (a) Energy as a function of y-position for an example betatron accelerated electron in a 1D simulation. (b) Energy as a function of y-position for an example electron accelerated by reconnection in a 2D simulation. Regions of betatron acceleration (I), X point acceleration (II), and plasmoid related acceleration (III) are visible.
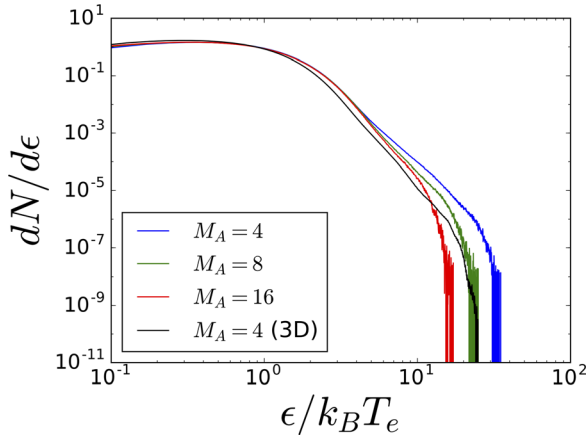
FIG. 7. Comparison of the electron energy spectra at $t/t_d = 0.25$ for three 2D simulations and one 3D simulation with $M_S = 2$ and M_A ranging from 4 to 16.

initial magnetic field amplitude is consistent with the reconnection electric field being primarily responsible for energizing the electrons, and the similar shapes of the spectra suggest the acceleration mechanisms are similar across these conditions. From the evolution of the spectra over the duration of the simulation we obtain an effective electric field E_{eff} energizing the electrons.[35] In all cases the effective electric field is $E_{eff} \approx 0.5 V_0 B_0$, which is consistent with the typical value of the reconnection electric field measured in the simulations. The effective electric field is slightly smaller in the 3D case, which is due to the electrons not being exposed to a uniform value of the reconnection electric field as they travel in the out-of-plane direction.

An estimate for the maximum electron energy can be obtained using the effective value of the reconnection electric field, $E_{eff} \approx 0.5 V_0 B_0$, and the fact that the maximum distance over which an electron can be accelerated is approximately the diameter of the bubble. In terms of experimentally tunable parameters, this gives $\epsilon_{max}/k_B T_e = (M_S^2/M_A)(R_b/(c/\omega_{pi}))$. These parameters can be chosen in future experiments to optimize the particle acceleration. For the parameters of the 3D simulation presented above, this expression gives $\epsilon_{max}/k_B T_e \approx 20$, which agrees with the location of the cutoff of the spectrum as shown in Figure 7. The condition for electrons to be accelerated by reconnection to suprathermal energies is then $(M_S^2/M_A)(R_b/(c/\omega_{pi})) > 1$, which is easily satisfied by

current laboratory conditions. Using the conditions of two laser-driven reconnection experiments performed at the Omega Laser Facility[24,41] which are estimated to be $M_S \approx 2.5, 5.6$, $M_A \approx 20, 9.2$, and $R_b/(c/\omega_{pi}) \approx 80, 22$, this model predicts maximum electron energies of $\epsilon_{max}/k_B T_e \approx 25, 75$. The electron temperatures in these experiments are typically 1 keV, so these would be 25–75 keV electrons.

G. Particle escape and impact of numerical parameters

The finite probability for a given electron to escape the system is another important factor that affects the shape of the spectrum. To determine the influence of particle escape, we perform 2D simulations with the configuration described in Sec. II where the system is periodic and infinite transverse to the plasma inflows, as shown in Figure 8(a). The spectrum for this configuration compared with the finite case previously discussed is shown in Figure 8(b), with both simulations having the conditions $M_S = 2$, $M_A = 4$, and $R = 27.5c/\omega_{pi}$. For the case of the infinite system, the high energy tail is steeper, contains more particles, and extends to higher energies, demonstrating the importance of particle escape for establishing the shape of the spectrum in the finite sized system. This also suggests that larger system sizes, such as may be produced in future experiments with more energetic laser drives, may provide more favorable conditions for measuring the particle acceleration.

To determine the influence of the numerical parameters that are not directly matched to their laboratory values due to computational expense, we have performed a set of simulations varying these parameters in the range $V_0/c = 0.025$–0.1 and $m_i/m_e Z = 32 - 512$. A comparison of the results of these simulations is shown in Figure 9. By the end of the simulation at $t/t_d = 0.5$, all simulations have formed a number of plasmoids in the range 6–8 and of similar size, as shown in Figs. 9(a)–9(c). The electron energy spectra for five simulations with different numerical parameters are given in Fig. 9(d), showing similar indices for the power-law tails and only small variations in the cutoff energy.

IV. EXPERIMENTAL SIGNATURES

The proposed model of particle acceleration for these systems predicts a number of important experimental signatures
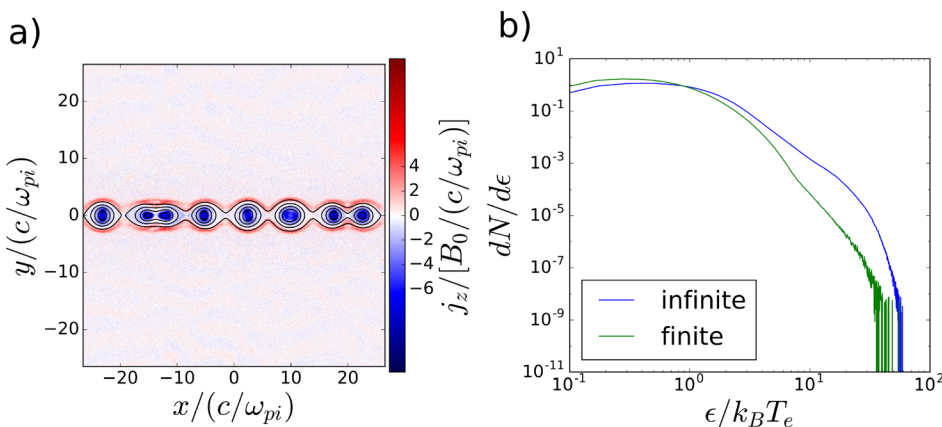

FIG. 8. (a) Out-of-plane current density j_z with overlaid magnetic field lines for a transversely infinite system simulation. (b) Comparison of the electron energy spectra for a transversely infinite simulation and a standard finite system simulation.

a) $\overline{V}=0.1, \overline{M}=128$

b) $\overline{V}=0.025, \overline{M}=128$

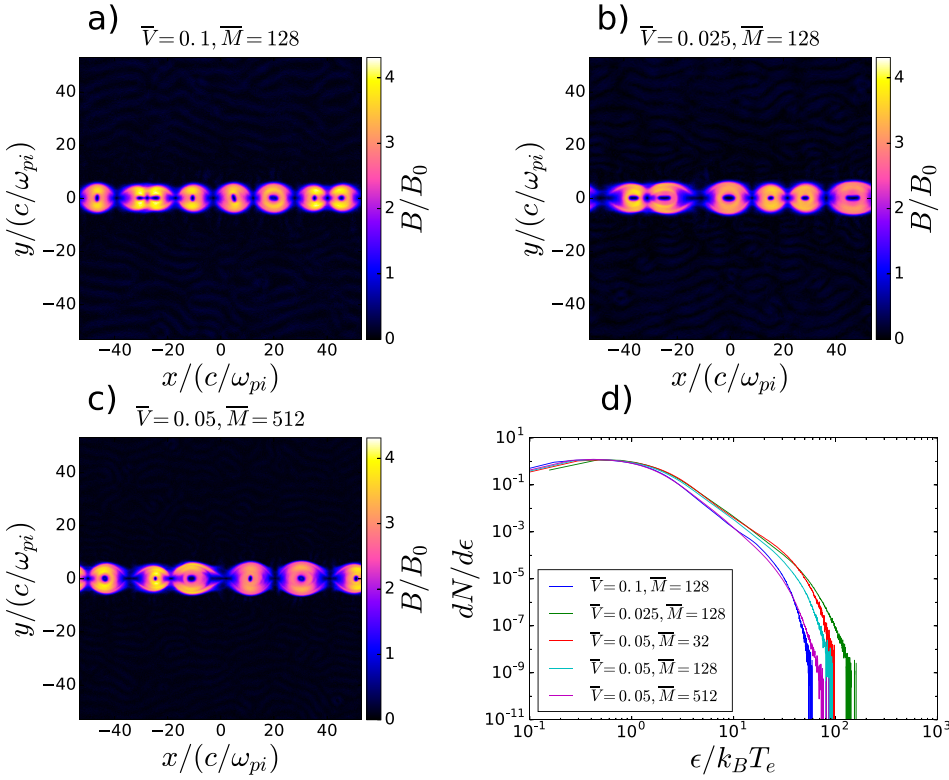c) $\overline{V}=0.05, \overline{M}=512$

d)

FIG. 9. (a)–(c) Magnitude of the magnetic field at $t/t_d = 0.5$ for three simulations with $M_S = 2$, $M_A = 4$, and $R/(c/\omega_{pi}) = 26.5$, but differing values for $\overline{V} = V_0/c$ and $\overline{M} = m_i/m_e Z$. (d) Electron energy spectra at $t/t_d = 0.5$ for five simulations with $M_S = 2$, $M_A = 4$, and $R/[(c/\omega_{pi})] = 26.5$, but differing numerical parameters in the range $\overline{V} = 0.025 - 0.1$ and $\overline{M} = 32 - 512$.

that could be used to identify the electrons accelerated by reconnection. Since the electrons are accelerated along the z-axis while being deflected by the in-plane magnetic field, the energetic electrons should escape the system in a fan-like profile, being emitted both in the direction of the reconnection outflows and in the direction opposite to that of the reconnection electric field. The most energetic electrons are expected to be those that are accelerated by the reconnection electric field over the longest distance, which would be those that start from the bottom of the system, are accelerated upwards, and escape nearly vertically. When the trajectories of the 1000 most energetic electrons from a 3D simulation are plotted (Figure 10) these features are clearly visible.
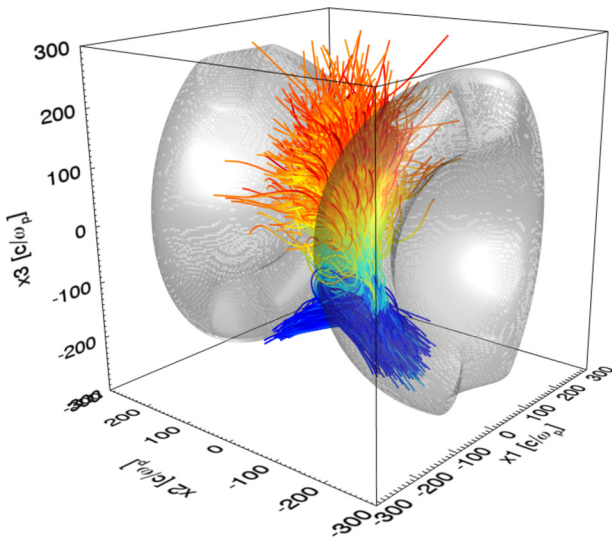

FIG. 10. Energetic electron trajectories, colored by energy, plotted over an isocontour of the magnetic field for a 3D simulation with $M_S = 2$ and $M_A = 4$.

The spectra previously presented have been integrated over all of the electrons initially in the plasma bubbles. To create synthetic spectra similar to what might be measured by a detector in an actual experiment, we calculate the pitch angle of each electron's velocity relative to the direction of the desired detector location and keep only those particles within a maximum acceptance angle, which we take to be $10°$. Figures 11(a) and 11(b) show the spectra obtained in this way for detectors receiving electrons from the $\pm x$ directions (reconnection outflows) and the $\pm z$ directions (parallel and antiparallel to the reconnection electric field). As expected, the detector receiving the electrons accelerated by the reconnection electric field shows a high energy component in the spectrum, whereas the detector on the opposing side does not. The detectors in the direction of the reconnection outflows show a high energy component but with fewer particles than for the $+z$ detector. The slight asymmetry between the $\pm x$ detectors is likely due to the motion of the plasmoid in the $+x$ direction, resulting in a bump at slightly higher energies in the spectrum for the $+x$ detector.

Figure 11(c) shows the distribution of energetic electrons with $\epsilon/k_B T_e \geq 15$ as a function of the direction of their velocity, parametrized by the azimuthal and polar angles θ and ϕ. This shows the expected features of energetic electrons escaping vertically (θ near 0) and in the reconnection outflows (ϕ near 0 and $\pm\pi$). The electrons escaping in the outflows have a significant divergence of their velocity angles, which is responsible for the lowering of the level of energetic electrons detected by the $\pm x$ detectors compared to the total spectrum. The typical angle of escape can be estimated for an electron energy of $\epsilon_{max}/2 = 1/2 m_e V_f^2$ as $\phi \approx V_0/V_f \approx \sqrt{M_A(Z m_e/m_i)(c/\omega_{pi})/R}$. This gives $\phi \approx 0.034$ for the reduced mass ratio used in the simulation,
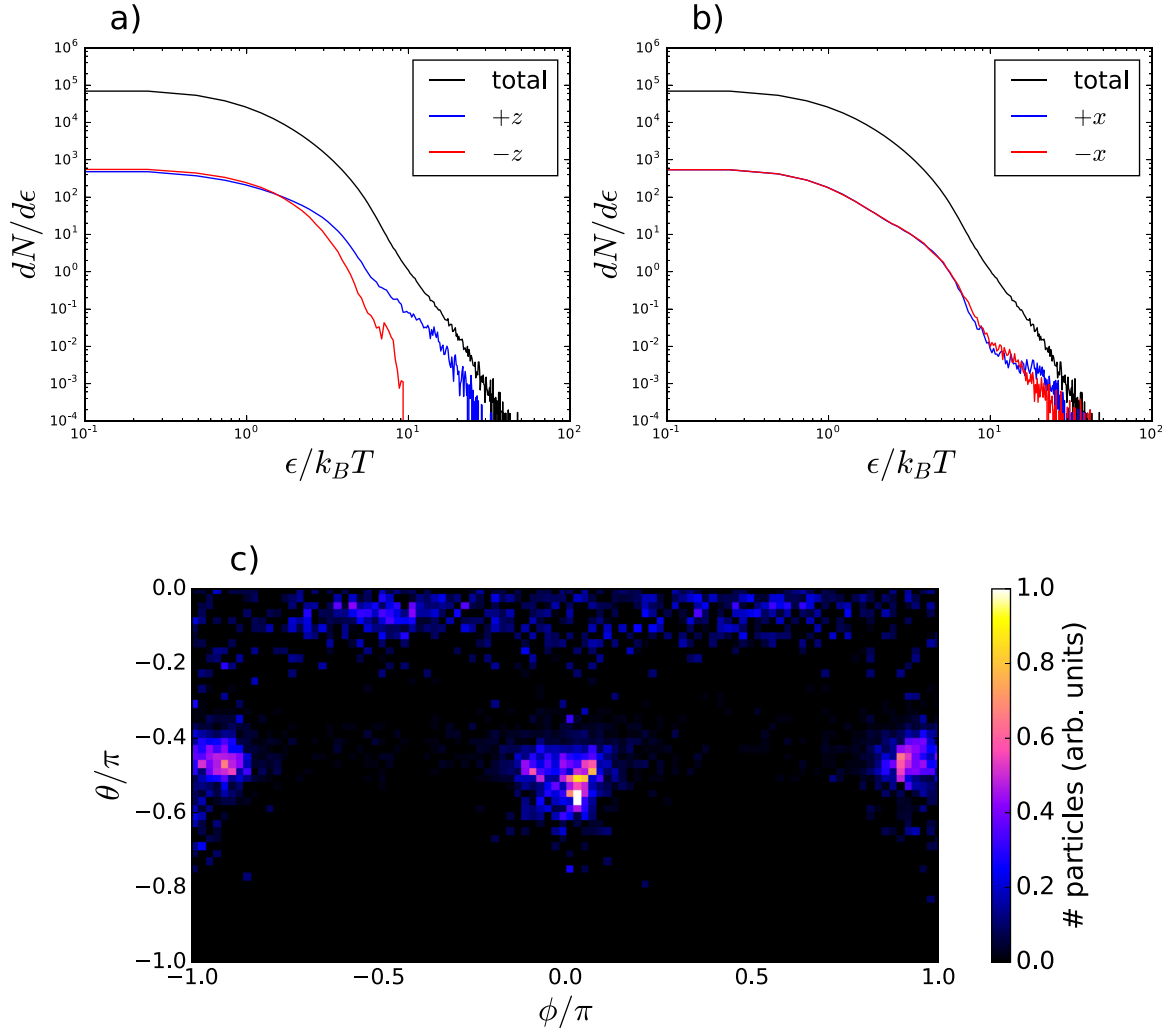
FIG. 11. Synthetic spectra measured by spectrometers receiving electrons traveling in the (a) $\pm z$ directions and (b) $\pm x$ directions with a 10° acceptance angle. (c) Distribution of velocity angle for electrons with $\epsilon/k_B T_e \geq 15$, where $\theta = 0$ corresponds to the $+z$ direction and $\phi = 0$ corresponds to the $+x$ direction.

which is in reasonable agreement with Fig. 11(c). Factors contributing to the underestimation are the intrinsic velocity divergence due to the radial bubble expansion and the broadening due to the in-plane magnetic field pulling escaping electrons away from the x-axis and towards the bubbles. For a realistic ratio of $m_i/m_e Z = 3672$ for fully ionized ions we estimate $\phi \approx 0.0065$, i.e., energetic electrons escape along the outflow axis.

V. CONCLUSIONS

In summary, by means of *ab initio* kinetic simulations of magnetic reconnection in laser-driven plasmas, we have shown that these systems can accelerate nonthermal electrons with sufficient energy and quantity to be detected in the conditions of current experiments. A nonthermal component that resembles a power-law spectrum is established as electrons are accelerated by the X points for varied amounts of time due to injection into and escape from the current layer. For the current experimental conditions a few plasmoids ($\sim 1 - 3$) can be formed, and particles trapped in the plasmoids can be further, but slowly, accelerated due to the electric field associated with the motion of the plasmoid. For the modeled plasma conditions we do not observe plasmoid

merging and the associated acceleration mechanisms. This would require significantly larger plasma bubbles, which may be produced at facilities like NIF and will be studied in future work. These results clearly indicate that laser-driven plasmas can play an important role in the study of particle acceleration induced by reconnection.

[1]E. G. Zweibel and M. Yamada, Annu. Rev. Astron. Astrophys. **47**, 291 (2009).

[2]H. Ji and W. Daughton, Phys. Plasmas **18**, 111207 (2011).

[3]A. S. Joglekar, A. G. R. Thomas, W. Fox, and A. Bhattacharjee, Phys. Rev. Lett. **112**, 105004 (2014); e-print arXiv:1507.03629v1.

[4]J. B. Taylor, Rev. Mod. Phys. **58**, 741 (1986).

[5]M. Hoshino and Y. Lyubarsky, Space Sci. Rev. **173**, 521 (2012).

[6]F. Guo, H. Li, W. Daughton, and Y. H. Liu, Phys. Rev. Lett. **113**, 155005 (2014).

[7]L. Sironi and A. Spitkovsky, Astrophys. J. **783**, L21 (2014); e-print arXiv:1401.5471.

[8]M. Oka, T.-D. Phan, S. Krucker, M. Fujimoto, and I. Shinohara, Astrophys. J. **714**, 915 (2010); e-print arXiv:1004.1154.

[9]X. R. Fu, Q. M. Lu, and S. Wang, Phys. Plasmas **13**, 012309 (2006).

[10]M. Hoshino, T. Mukai, T. Terasawa, and I. Shinohara, J. Geophys. Res. **106**, 25979, doi:10.1029/2001JA900052 (2001).

[11]J. F. Drake, M. Swisdak, H. Che, and M. A. Shay, Nature **443**, 553 (2006).

[12]J. T. Dahlin, J. F. Drake, and M. Swisdak, Phys. Plasmas **21**, 092304 (2014); e-print arXiv:1406.0831.

[13]N. F. Loureiro, A. A. Schekochihin, and S. C. Cowley, Phys. Plasmas **14**, 100703 (2007); e-print arXiv:0703631 [astro-ph].

[14]K. Nalewajko, J. Zrake, Y. Yuan, W. E. East, and R. D. Blandford, Astrophys. J. **826**, 115 (2016); e-print arXiv:1603.04850.

[15]D. D. Ryutov, R. P. Drake, and B. A. Remington, Astrophys. J., Suppl. Ser. **127**, 465 (2000).

[16]D. D. Ryutov, N. L. Kugland, H. S. Park, C. Plechaty, B. A. Remington, and J. S. Ross, Plasma Phys. Controlled Fusion **54**, 105021 (2012).

[17]B. A. Remington, R. P. Drake, and D. D. Ryutov, Rev. Mod. Phys. **78**, 755 (2006).

[18]P. M. Nilson, L. Willingale, M. C. Kaluza, C. Kamperidis, S. Minardi, M. S. Wei, P. Fernandes, M. Notley, S. Bandyopadhyay, M. Sherlock, R. J. Kingham, M. Tatarakis, Z. Najmudin, W. Rozmus, R. G. Evans, M. G. Haines, A. E. Dangor, and K. Krushelnick, Phys. Rev. Lett. **97**, 255001 (2006).

[19]C. K. Li, F. H. Séguin, J. A. Frenje, J. R. Rygg, R. D. Petrasso, R. P. J. Town, O. L. Landen, J. P. Knauer, and V. A. Smalyuk, Phys. Rev. Lett. **99**, 055001 (2007).

[20]P. M. Nilson, L. Willingale, M. C. Kaluza, C. Kamperidis, S. Minardi, M. S. Wei, P. Fernandes, M. Notley, S. Bandyopadhyay, M. Sherlock, R. J. Kingham, M. Tatarakis, Z. Najmudin, W. Rozmus, R. G. Evans, M. G. Haines, A. E. Dangor, and K. Krushelnick, Phys. Plasmas **15**, 092701 (2008).

[21]L. Willingale, P. M. Nilson, M. C. Kaluza, A. E. Dangor, R. G. Evans, P. Fernandes, M. G. Haines, C. Kamperidis, R. J. Kingham, C. P. Ridgers, M. Sherlock, A. G. R. Thomas, M. S. Wei, Z. Najmudin, K. Krushelnick, S. Bandyopadhyay, M. Notley, S. Minardi, M. Tatarakis, and W. Rozmus, Phys. Plasmas **17**, 043104 (2010).

[22]J. Zhong, Y. Li, X. Wang, J. Wang, Q. Dong, C. Xiao, S. Wang, X. Liu, L. Zhang, L. An, F. Wang, J. Zhu, Y. Gu, X. He, G. Zhao, and J. Zhang, Nat. Phys. **6**, 984 (2010).

[23]Q. L. Dong, S. J. Wang, Q. M. Lu, C. Huang, D. W. Yuan, X. Liu, X. X. Lin, Y. T. Li, H. G. Wei, J. Y. Zhong, J. R. Shi, S. E. Jiang, Y. K. Ding, B. B. Jiang, K. Du, X. T. He, M. Y. Yu, C. S. Liu, S. Wang, Y. J. Tang, J. Q.

Zhu, G. Zhao, Z. M. Sheng, and J. Zhang, Phys. Rev. Lett. **108**, 215001 (2012); e-print arXiv:1203.4036v1.

[24]G. Fiksel, W. Fox, A. Bhattacharjee, D. H. Barnak, P.-Y. Chang, K. Germaschewski, S. X. Hu, and P. M. Nilson, Phys. Rev. Lett. **113**, 105003 (2014).

[25]M. J. Rosenberg, C. K. Li, W. Fox, A. B. Zylstra, C. Stoeckl, F. H. Séguin, J. A. Frenje, and R. D. Petrasso, Phys. Rev. Lett. **114**, 205004 (2015).

[26]M. Rosenberg, C. Li, W. Fox, I. Igumenshchev, F. Séguin, R. Town, J. Frenje, C. Stoeckl, V. Glebov, and R. Petrasso, Nat. Commun. **6**, 6190 (2015).

[27]M. Yamada, R. Kulsrud, and H. Ji, Rev. Mod. Phys. **82**, 603 (2010).

[28]M. Haines, Phys. Rev. Lett. **78**, 254 (1997).

[29]J. A. Stamper, Laser Part. Beams **9**, 841 (1991).

[30]L. Gao, P. M. Nilson, I. V. Igumenshchev, M. G. Haines, D. H. Froula, R. Betti, and D. D. Meyerhofer, Phys. Rev. Lett. **114**, 215003 (2015).

[31]R. G. Hemker, e-print arXiv:1503.00276.

[32]R. A. Fonseca, L. O. Silva, F. S. Tsung, V. K. Decyk, W. Lu, C. Ren, W. B. Mori, S. Deng, S. Lee, T. Katsouleas, and J. C. Adam, Lect. Notes Comput. Sci. **2331**, 342 (2002).

[33]R. A. Fonseca, S. F. Martins, L. O. Silva, J. W. Tonge, F. S. Tsung, and W. B. Mori, Plasma Phys. Controlled Fusion **50**, 124034 (2008); e-print arXiv:0810.2460.

[34]R. A. Fonseca, J. Vieira, F. Fiuza, A. Davidson, F. S. Tsung, W. B. Mori, and L. O. Silva, Plasma Phys. Controlled Fusion **55**, 124011 (2013); e-print arXiv:1310.0930.

[35]S. R. Totorica, T. Abel, and F. Fiuza, Phys. Rev. Lett. **116**, 095003 (2016); e-print arXiv:1601.05845.

[36]J. M. Dawson, Rev. Mod. Phys. **55**, 403 (1983).

[37]T. Takizuka and H. Abe, J. Comput. Phys. **25**, 205 (1977).

[38]K. Nanbu and S. Yonemura, J. Comput. Phys. **145**, 639 (1998).

[39]D. D. Ryutov, N. L. Kugland, M. C. Levy, C. Plechaty, J. S. Ross, and H. S. Park, Phys. Plasmas **20**, 032703 (2013).

[40]W. Fox, A. Bhattacharjee, and K. Germaschewski, Phys. Rev. Lett. **106**, 215003 (2011); e-print arXiv:1104.0605.

[41]W. Fox, A. Bhattacharjee, and K. Germaschewski, Phys. Plasmas **19**, 056309 (2012).

[42]S. Lu, Q. Lu, Q. Dong, C. Huang, S. Wang, J. Zhu, Z. Sheng, and J. Zhang, Phys. Plasmas **20**, 112110 (2013).

[43]S. Lu, Q. Lu, C. Huang, Q. Dong, J. Zhu, Z. Sheng, S. Wang, and J. Zhang, New J. Phys. **16**, 083021 (2014).

[44]K. M. Schoeffler, N. F. Loureiro, R. A. Fonseca, and L. O. Silva, Phys. Rev. Lett. **112**, 175001 (2014).

[45]K. M. Schoeffler, N. F. Loureiro, R. A. Fonseca, and L. O. Silva, Phys. Plasmas **23**, 056304 (2016).

[46]J.-L. Vay, J. Comput. Phys. **165**, 511 (2000).

[47]P. L. Pritchett, J. Geophys. Res.: Space Phys. **106**, 3783, doi:10.1029/1999JA001006 (2001).

[48]P. L. Pritchett, F. V. Coroniti, R. Pellat, and H. Karimabadi, J. Geophys. Res. **96**, 11523, doi:10.1029/91JA01094 (1991).

[49]E. Fermi, Phys. Rev. **75**, 1169 (1949); e-print arXiv:0707.2783v2.

[50]T. G. Northrop, Rev. Geophys. **1**, 283, doi:10.1029/RG001i003p00283 (1963).

[51]S. Lu, Q. Lu, F. Guo, Z. Sheng, H. Wang, and S. Wang, New J. Phys. **18**, 13051 (2016).